Nanoscale

PAPER

View Article Online
View Journal | View Issue

Cite this: *Nanoscale*, 2017, **9**, 3834

Stretchable electronic skin based on silver nanowire composite fiber electrodes for sensing pressure, proximity, and multidirectional strain†

Yin Cheng, Ranran Wang,* Haitao Zhai and Jing Sun*

Received 5th January 2017,
Accepted 14th February 2017

DOI: 10.1039/c7nr00121e

rsc.li/nanoscale

Electronic skin (E-skin) has been attracting great research interest and effort due to its potential applications in wearable health monitoring, smart prosthetics, robot skins and so on. To expand its applications, two key challenges lie in the realization of device stretchability, and independent sensing of pressure and multidirectional lateral strain. Here we made a combination of rational device structure and artfully engineered sensing materials to fulfill the mentioned demands. The as-prepared E-skin took a simple orthogonal configuration to enable both capacitive mode for pressure sensing and resistive mode for multidirectional strain sensing, independently. Pre-cracked silver nanowire based fibers with helical microstructures were utilized as basic electrodes to endow the E-skin with intrinsic stretchability and strain sensing capability. Through dielectric layer optimization, the pressure sensing sensitivity was greatly enhanced, with a detection limit of 1.5 Pa. For application demonstrations, we utilized the E-skin as both flat and curved platforms for pressure mapping, and also as human motion sensors, such as palm and thumb bending.

1. Introduction

In recent years, researchers have been increasingly focusing on the investigation of electronic skin (E-skin), which basically emulates the functions of human skin to sense various environmental stimuli, as E-skins hold great application promise in wearable health monitoring, smart prosthetics, advanced robot skins, and intelligent human–machine interactions.[1–9] In the mechanical stimuli sensing, normal pressure and lateral strain are two key elements: normal pressure detection helps to realize the grasp control, object manipulation, and orientation determination;[10,11] while tensile strain monitoring facilitates the enhancement of proprioception, especially at the joint positions.[12] For pressure sensing, several sensing mechanisms have been employed, including piezoresistive,[13–16] piezoelectric,[17] triboelectric,[18,19] and capacitive[20–25] technologies. A capacitive pressure sensor is considered as a promising candidate due to its simple structure design, facile fabrication and excellent comprehensive properties. Bao *et al.* creatively took advantage of a microstructured elastomeric dielectric layer to greatly improve the sensitivity and response speed.[26] As strain sensing is essential for human motion perception and manoeuvrability,[27–32] it is highly demanded to incorporate lateral strain sensing capability into the E-skin to expand its application fields. To this end, there are two strategies commonly used. One is to directly correlate the capacitance variation with the lateral strain, *via* leveraging Poisson's ratio contraction of the thickness.[23,24,33–37] However, both the intrinsically limited sensitivity (gauge factor value within 1)[30,36] and the difficulty in distinguishing a response signal from that induced by pressure hinder its practical applications. The other method is adding a dedicated sensing element for strain detection in each pixel.[38,39] Obviously, this complicates the structure design and fabrication process, and also results in a bulkier device. Except for the multiple mechanical stimuli sensing ability, stretchability is another hard-to-achieve and yet crucial feature as it renders the E-skin capable of attaching conformably onto arbitrarily curved and moving surfaces such as joints of human and robots, and also allows the E-skin to tolerate frequent and prolonged mechanical impacts such as bending and twisting. In general, to overcome the formidable challenges mentioned above, a combination of rational device architecture and artfully engineered sensing materials is urgently needed to enable an intrinsically stretchable E-skin to sense multiple kinds of mechanical stimuli, such as normal pressure, omnidirectional lateral strain, and approaching/touching.

State Key Laboratory of High Performance Ceramics and Superfine Microstructure, Shanghai Institute of Ceramics, Chinese Academy of Sciences, Shanghai 200050, China. E-mail: wangranran@mail.sic.ac.cn, jingsun@mail.sic.ac.cn

†Electronic supplementary information (ESI) available. See DOI: 10.1039/c7nr00121e

Herein, we described a highly sensitive, stretchable and wearable E-skin capable of sensing multiple mechanical stimuli with a single set of sensing materials, such as pressure, lateral strain and approaching/touching. Pre-cracked elastic conductive fibers based on silver nanowires (AgNWs) were exploited as basic electrodes to form a point-to-point capacitor matrix, using elastomers as dielectric and substrate layers. The optimized E-skin sensor exhibited excellent pressure sensing performance, including a wide dynamic sensing range of 0–50 kPa and an ultralow detection limit of 1.5 Pa. Besides, the detection of human finger approaching/touching was successfully performed through a fringing electric field mechanism. Furthermore, the pre-cracked fiber electrodes endowed the E-skin with planar strain sensing capability and also worth noting is that the lateral strain direction could be determined by virtue of the orthogonally aligned fiber electrode configuration. To demonstrate its great application potential, we used the E-skin as a pressure sensing platform to intuitively map the pressure distribution of rubber pieces. Also the highly flexible feature of the E-skin allowed it to conform well to a glass bottle, while maintaining the pressure sensing function. Lastly, to make the most of the multidirectional lateral strain sensing ability, the E-skin was adhered tightly to the back of human hand, as expected the thumb bending and palm bending could be traced and clearly differentiated. Our E-skin stands out with three main highlights: (i) a pre-cracked fiber with a helical microstructure was utilized as a basic electrode to realize both stretchability and strain sensing capability of the E-skin; (ii) a simple crisscross device configuration was adopted to enable both capacitive mode for pressure sensing and resistive mode for multidirectional strain sensing, independently; (iii) the dielectric layer was optimized to improve the pressure sensing sensitivity.

2. Results and discussion

Fig. 1a–c show the schematic illustration of the E-skin structure and the pre-cracked fiber electrode. The elastomeric dielectric layer (D-layer) is sandwiched between two electrode layers (E-layers, pre-cracked fibers aligned in parallel and embedded in an elastomeric matrix), and encapsulated in two

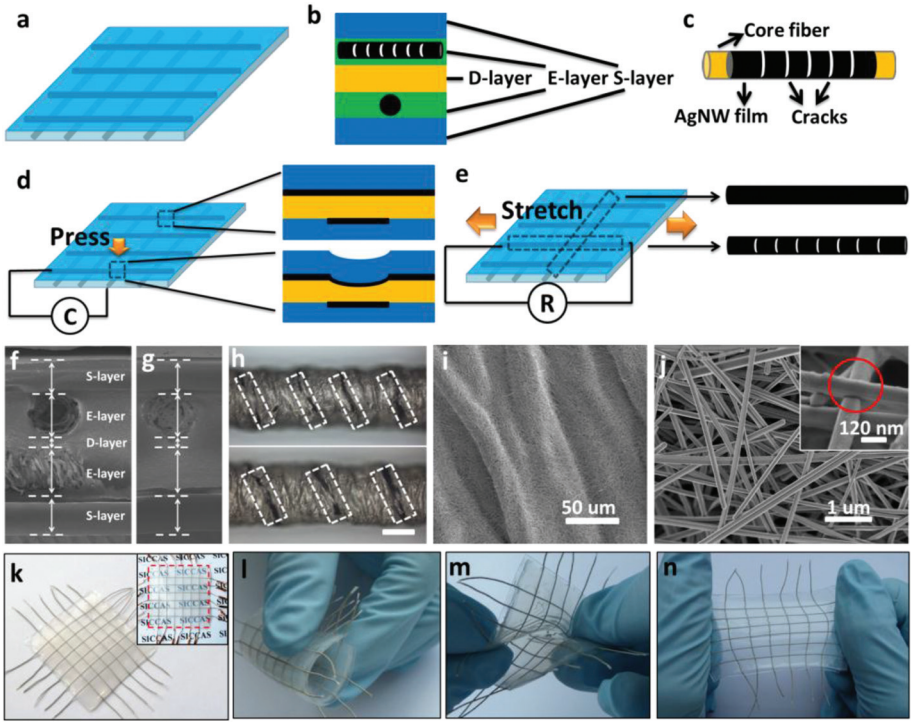

Fig. 1 The pre-cracked fiber electrode and the piezocapacitive E-skin device. (a) Schematic of the E-skin assembly. (b) Schematic of the cross section at the crisscross position of the E-skin. (c) Schematic of the pre-cracked fiber. (d) Schematic of the pressure sensing mechanism. The pressing position shows a decrease in the thickness of the D-layer. (e) Schematic of the strain sensing mechanism. The strain component along the pre-cracked fiber caused an increase in crack density. SEM images of the cross section at crisscross (f) and none crisscross (g) positions. The thicknesses of the S-layer, E-layer and D-layer are 270 μm, 350 μm, and 75 μm. (h) Optical images of the pre-cracked fiber (5 dip-coating times) at the original (top) and stretched (bottom, strain of 30%) conditions. The cracks (marked within a white dotted box) grow wider when being stretched. Scale bar, 200 μm. (i) Low magnification SEM image of the AgNW network on the surface of SCY (5 dip-coating times), showing a blanket-like AgNW film with a wavy configuration. (j) High magnification SEM image of the AgNW network after the annealing treatment, the inset shows the nanowelding effect at the junction position (marked by red circle). (k) The photograph of the fabricated E-skin device (6 × 6 arrays, pitch size of the sensing matrix is 5 mm, size of the E-skin device is 4.5 cm × 4.5 cm) and the inset shows the E-skin on a paper with words to show its semi-transparent feature. The E-skin was bended (l), twisted (m), and stretched to a strain of ~50% (n).

polydimethylsiloxane (PDMS) substrate layers (S-layers). The two E-layers are face to face orthogonally to form point-to-point capacitor pixels at the crisscross locations. The fabrication of the E-skin is based on a facile and scalable layer-by-layer assembly strategy (detailed fabrication steps in the Experimental section). Our E-skin succeeded in combining a delicate design of the device structure and artfully engineered sensing elements to realize both pressure and strain sensing, independently. As seen in Fig. 1d, the two orthogonally face-to-face E-layer configurations formed a capacitor matrix of sensing pixels (simplified as parallel plate capacitors); when pressure was applied on a sensing pixel, the corresponding dielectric layer went through a thickness decrease, which induced the capacitance increase and consequently captured the pressure. In Fig. 1e, when the E-skin was stretched, the plane strain component parallel to the pre-cracked fibers resulted in a crack density increase which caused a linear resistance increase, while that perpendicular to the pre-cracked fibers barely influenced the crack density. In this way, the amplitude and direction of the applied strain could be determined. The scanning electron microscopy (SEM) images in Fig. 1f (crisscross position) and 1g (none crisscross position) revealed each layer clearly, with the D-layer being ~75 μm and the whole E-skin film being ~1.3 mm. Through optical microscopy, the morphologies of the pre-cracked fiber at the original (top image in Fig. 1h) and stretched (bottom image in Fig. 1h, strain of 30%) conditions are presented. The pre-cracking processing was adopted deliberately to obtain strain-sensing capability (discussed in the later part). The pre-cracked fiber (detailed fabrication information in the Experimental section) comprises a single covered yarn (SCY, a polyurethane (PU) fiber twined helically by a layer of polyester (PE) yarn, more structural details in Fig. S1, ESI†) as the highly elastic scaffold core fiber (diameter of 350 μm, ultimate tensile strain of up to 400%) and the AgNW (morphology characterization in Fig. S2, ESI†) film on the surface of the PE yarn as the conductive network. The AgNWs were coated through a dip-coating methodology, similar to the "dyeing" technique in the textile industry and frequently utilized for the fabrication of electronic textiles.[40–43] The AgNW network density on the surface of the SCY (SEM characterization in Fig. S3, ESI†) and the conductivity of the resultant fibers (Fig. S4, ESI†) could be tuned with ease *via* the dip-coating times. The SEM image in Fig. 1i indicates that the AgNW network on the surface of the SCY forms a continuous blanket-like film with a wavy configuration, coating highly conformably onto the underlying PE yarns. Subsequent to the dip-coating step, an annealing treatment was implemented to further promote the conductivity and mechanical robustness of the AgNW network through the nanowelding effect at the network junctions as shown in Fig. 1j and S5 in the ESI.† Fig. 1k shows the photograph of the E-skin device (6 × 6 arrays, pitch size of 5 mm) and its semi-transparent feature (inset in Fig. 1k). Owing to the thin film structure and intrinsically stretchable component materials, the E-skin is highly mechanically flexible and stretchable, thus it could be bended (Fig. 1l), twisted (Fig. 1m), and even stretched (Fig. 1n) with no delamination and damage phenomena. This valuable virtue ensures that the E-skin is highly suitable for human–machine interactions, smart prosthetics, and robot skins, wherein frequent mechanical impacts are inevitable.

To investigate the pressure sensing properties, a customized force gauge containing a long plastic pole terminated with a square-shaped glass sheet (5 mm × 5 mm) was used to apply normal pressure onto the center of a sensing pixel on the E-skin. Fig. 2a shows the relative capacitance variations of three E-skin samples along with the pressure up to 50 kPa. The three E-skin samples differed from each other in material choice of the D-layer, including PDMS, Dragon skin 10, and Ecoflex 00-30, respectively (detailed material information in Table S1, ESI†). All the three samples exhibited a similar response tendency: a monotonic capacitance increase caused by a decrease in the D-layer thickness due to the increasing normal pressure, accompanied by a transition section between two quasi-linear sections, wherein the slope of the curves (defined as the pressure sensing sensitivity, S) started to decline sharply as a result of the compressive strain hardening effect.[44] Among the three samples, the E-skin with a D-layer of Ecoflex 00-30 has the highest sensitivity (S being 0.096 kPa^{-1} at the low pressure section below 0.1 kPa, and 1.1 MPa^{-1} at the high pressure section above 10 kPa), which is attributed to the lowest elastic modulus (EM) of the D-layer (Ecoflex 00-30: ~0.069 MPa; Dragon Skin 10: ~0.152 MPa; PDMS: ~5 MPa). This sensitivity improvement mechanism (see detailed pressure sensing mechanism analysis in the ESI†) is explained by using eqn (1):

$$\frac{\Delta C}{C_0} = \frac{P}{E - P}. \quad (1)$$

Here C_0 and ΔC are the initial and incremental capacitances, respectively; P is the normal pressure applied to the E-skin; E is the elastic modulus of the corresponding D-layer. The sensitivity enhancement strategy *via* choosing a low EM material as the D-layer has an advantage of a more compact structure over the methodology of the microstructured D-layer placed in between two E-layers. Besides, the latter design carries inherent drawbacks such as that the gas phase in the D-layer brings about erratic baseline, hysteresis, and irreproducible sensitivity,[37] and it also involves complicated MEMS fabricating processes including photolithography, etching, *etc.*[26,45] The E-skin with a D-layer of Ecoflex 00-30 was selected as the optimal sample for further investigation. To evaluate the reproducibility of pressure sensing performance, we recorded the signal response when 15 consecutive step pressures ranging from 110 to 5100 Pa were applied as seen in Fig. 2b, and the highly stable and consistent response signals confirmed excellent reproducibility. In order to determine the detection limit, ultralow step pressures were input to collect the response signals, and a detection limit of 1.5 Pa was obtained as seen in Fig. 2c, which was comparable to the best results reported.[13,46–48] The response time is another key parameter for E-skin sensing, and the real-time capacitance vari-

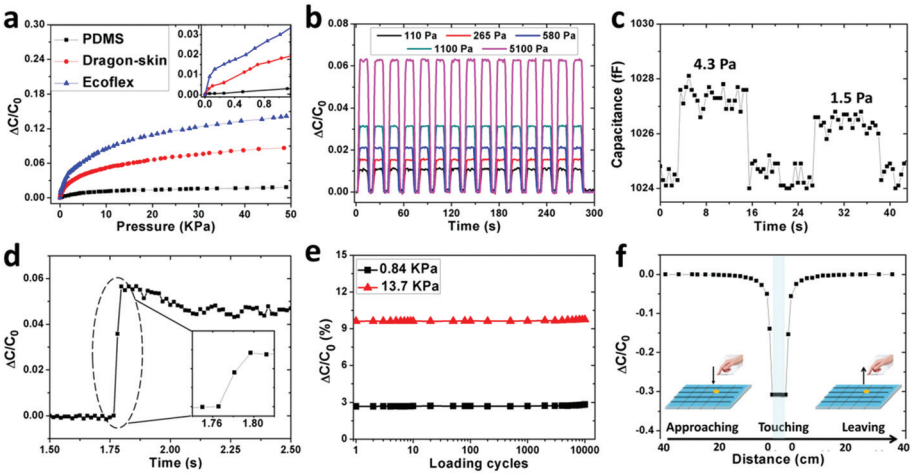

Fig. 2 The pressure sensing properties of the E-skin. (a) The relative capacitance variation *versus* the applied pressure up to 50 kPa of three E-skin samples with different D-layers, including PDMS, Dragon skin 10, and Ecoflex 00-30, respectively. The inset shows the response curves at the low pressure regime of within 1 kPa. (b) The relative capacitance variation of the E-skin when 15 consecutive step pressures ranging from 110 to 5100 Pa were applied. (c) The capacitance variation of the E-skin when ultralow step pressures (4.3 Pa and 1.5 Pa) were applied to determine the detection limit. (d) The real-time (time resolution of 15.625 ms) capacitance variation when a rubber cubic was dropped from above (~1 mm) the center of a sensing pixel. The static pressure caused by the rubber cubic was about 1.5 kPa. The inset shows the close-up of the signal response part. (e) Durability test of the E-skin. The relative capacitance variation at pressures of 0.84 kPa and 13.7 kPa up to 10 000 loading cycles. (f) The capacitance variation of the E-skin when a human finger approached, touched and then left a sensing pixel. The insets show the schematics of the finger approaching and leaving.

ation was recorded when a rubber cube was dropped onto a sensing pixel. In Fig. 2d, we captured a fast response time of ~32 ms, which stood comparison with that of human skin (30–50 ms),[49] and subsequent small response signal overshoot and settling, which corresponded to the kinetic motion of the falling object, including a pressure overshoot and rebounding.[2] Good durability is always an indispensable aspect for practical and long-term applications, so we implemented a cyclic pressing test with the aid of a high-precision motorized linear stage (see the Experimental section for detailed information). As seen in Fig. 2e, the capacitance variations at pressures of 0.84 kPa and 13.7 kPa were plotted up to 10 000 cycles, and exhibited a fairly stable response signal, with the signal drifts at 0.84 kPa and 13.7 kPa after 10 000 cycles being only 4.6% and 3.8% respectively. Apart from pressure sensing, proximity/touching sensing is a meaningful complementary function of the E-skin, particularly in applications such as smart robots and intelligent human–machine interactions,[20] for example, to help the robot to "see" the approaching object for collision avoidance. Fig. 2f shows the capacitance variation along with a human finger approaching the center of a sensing pixel and leaving, vertically above the pixel. Clearly, during the approaching process, the capacitance started to decrease slowly within a distance of 20 cm, and then dropped sharply within a distance of 10 cm. The capacitance declined to the lowest level when the finger touched the E-skin and the leaving process caused the same response curve as that of approaching. This approaching/touching sensing was attributed to the interception and shunting to ground of the fringing electric field above the sensing pixel by the finger (see the detailed mechanism analysis in the ESI†).

To endow the E-skin with lateral strain sensing capability, we deliberately engineered the SCY-AgNW fiber electrodes by pre-cracking the AgNW film on the surface. To pre-crack the fiber electrode, the fiber was first stretched to a strain of 40% and then released to the original state, to generate evenly distributed cracks on the AgNW film (as shown in Fig. 1h). Fig. 3a presents the relative resistance variation of the fiber electrodes when the E-skin was stretched (parallel to the fiber axis) up to the strain of 30%. The fiber electrode before pre-cracking showed an almost constant resistance within the strain of 10% and then a linear resistance increase. However, the fiber electrode after pre-cracking exhibited a linear resistance increase throughout the strain range, and the gauge factor was ~3.2 (defined as the slope of the curve), much higher than that of E-skins based on capacitive mode (maximum of 1).[24,30,37] To understand this difference, we traced the microstructure variation of the fiber electrode during the first stretching up to a strain of 50% (Fig. S6, ESI†). We found no cracks on the surface of the AgNW film within a strain of 10%, and cracks started to appear and the number of cracks increased as the strain increased. At the strain of 50%, the AgNW film was already severely damaged, which was undesirable. We believed it was the blanket-like wavy configuration of the AgNW film on the PE fibers (shown in Fig. 1i) that allowed the resistance maintenance within a strain of 10% as the wavy configuration extended to a more planar configuration to absorb the tensile strain. After that, cracks were generated to accommodate further stretching. For comparison, the crack density of the fiber electrode was counted during the stretching process before and after pre-cracking (Fig. S7, ESI†). Interestingly, the variation trends of the crack density were highly consistent

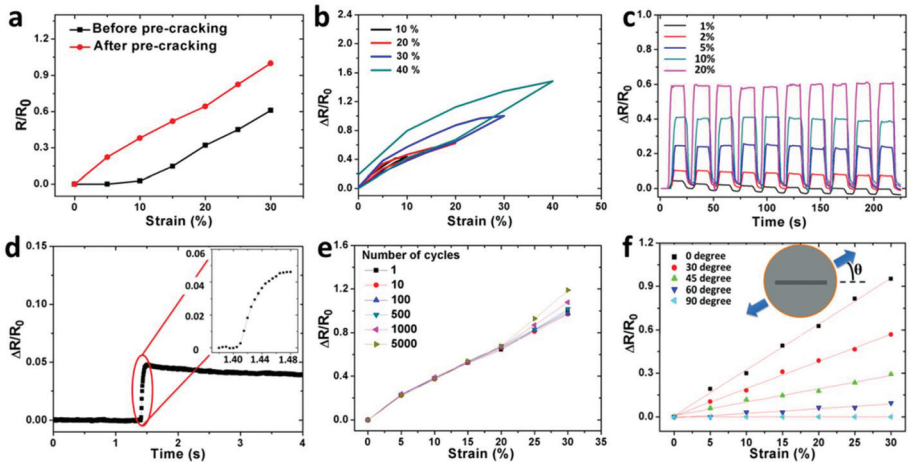

Fig. 3 Strain sensing properties of the E-skin. (a) The relative resistance variation of the fiber electrodes before and after pre-cracking. (b) The response curves of the stretching–releasing process at ultimate strains of 10%, 20%, 30% and 40%. (c) The resistance variation of the E-skin when 10 consecutive step strains ranging from 1% to 20% were input. (d) The real-time (time resolution of 5 ms) signal response when a quasi-transient step strain (1%) was input. (e) The relative resistance variation curves when cyclic stretching up to a strain of 30% for 5000 times was conducted. (f) The relative resistance variation *versus* multidirectional strain input, varying from 0 to 90 degree. The inset shows the schematic of the strain applied on the disk-shaped E-layer in the direction of θ.

with that of the relative resistance variation as shown in Fig. 3a, indicating the dependence of the resistance variation on the crack density. Obviously, the pre-cracking process led to a linear crack number increase throughout the strain range of 30% in the subsequent loading cycles, thus creating a desirable linear resistance change along with the strain increase. In fact, this pre-cracking scheme was similar to the strategy that was harnessed to obtain highly sensitive sensors *via* mimicking the spider sensory system.[50–52] Specifically, to obtain stretchable sensors, cracks in the conductive layers were more preferred to enable distinct resistance variation along with the applied strain, and a larger crack density contributed to larger sensitivity, as long as the crack density change was reproducible in the sensing range. In our work, we deliberately engineered cracks on the surface of the fiber electrode to endow strain sensing capability, on the condition that the conductive fiber electrodes could maintain the pressure sensing function.

We further investigated the strain sensing performance of the E-skin with pre-cracked fiber electrodes. Fig. 3b shows the response curves of the stretch-release process at ultimate strains of 10%, 20%, 30% and 40%, and obvious hysteresis started to appear when the ultimate strain increased to 30%, probably due to considerable hysteresis of the silicone rubber matrix of E-layers.[53] When the ultimate strain increased to 40%, an irreversible resistance increase occurred after a loading–unloading cycle, suggesting an irrecoverable damage to the AgNW network. In Fig. 3c, the resistance variations of the E-skin were recorded when 10 consecutive step strains ranging from 1% to 20% were input, the results confirmed a low detection limit of 1% and also excellent reproducibility of strain sensing performance, which we assumed was due to the stable crack generation memory at specific strains in each cycle. To determine the response time of strain sensing (detailed information in the Experimental section), we input a quasi-transient step strain (1%) and recorded the real-time (time resolution of 5 ms) signal response (Fig. 3d); the response time was captured to be as fast as ~70 ms, which allowed the monitoring of a vast majority of human motions.[27,29] Fig. 3e shows the response curves when cyclic stretching up to a strain of 30% for 5000 times was conducted; the results revealed signal drifts of 5% and 15% at strains of 20% and 30% respectively after 5000 loading cycles, proving a reliable durability. Also, note that the resistance variation signal responded exclusively to the applied lateral strain, rather than being interfered with by the pressure simultaneously, as in the case of a strain sensor based on capacitive mode. The resistance variation output signal caused by the pressure input could be neglected reasonably compared with that corresponding to the strain input (Fig. S8, ESI†).

To better emulate the human skin, it is of great significance, yet quite challenging, to make the E-skin able to detect multidimensional planar strain, which will open up future wearable device applications that require both monitoring and controlling of various surface conditions in human skin, mechanical structures, and soft robotics.[54] Fortunately, the orthogonally aligned fiber electrode configuration endowed our E-skin with the capability of determining the lateral strain direction. To investigate the multidirectional strain sensing properties, a disk-shaped E-layer was designed (the fabrication process in the Experimental section) to test the resistance change *versus* multidirectional strain, the angle between the stretching direction and the axial direction of the fiber electrode varying from 0 to 90 degree (Fig. S9, ESI†). Fig. 3f shows the testing results: all the response curves displayed linear correlations between resistance and strain increase, and the gauge factor of strain sensing decreased as the strain direction

increased, being 3.2 in the direction of 0 degree and 0 in the direction of 90 degree. The dependence of strain sensing sensitivity on the strain direction complied well with the plane strain transformation principles (see the multidirectional strain sensing mechanism in the ESI†). In this way, for a randomly applied lateral strain on the E-skin, the direction and amplitude of this maximum principal strain can be determined easily by analyzing the amplitude ratio of the two orthogonally aligned fiber electrodes' output signal (see the multidirectional strain sensing mechanism in the ESI†).

To demonstrate the potential use of the E-skin as a pressure sensing platform, three rubber pieces with letter shapes (letters of "C", "A", and "S") were placed on the flat surface of the E-skin (Fig. 4a–c). The output capacitance variation of each sensing pixel was recorded and plotted, displaying the spatial distribution of the pressure through color contrast mapping as

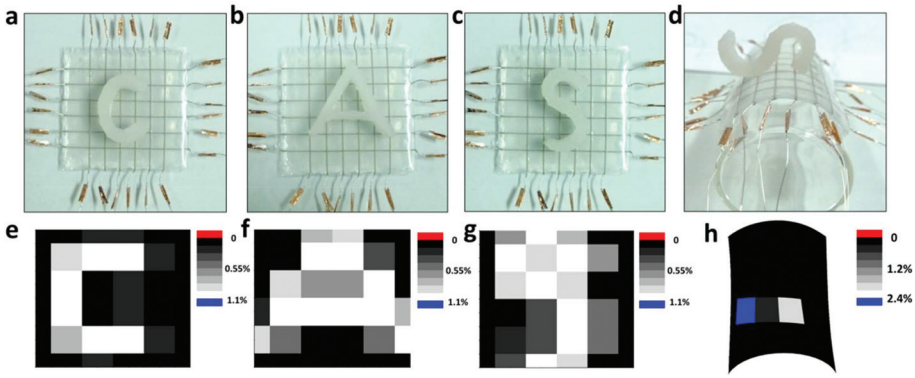

Fig. 4 The E-skin device as a pressure sensing platform. Rubber pieces with letter shapes of "C" (a), "A" (b), and "S" (c) were placed on the flat surface of the E-skin. A rubber piece with the letter shape of "S" (d) was placed on the curved surface of the E-skin, which was adhered onto the outer surface of a round glass bottle (diameter of 3 cm). The spatial pressure distribution on the E-skin by means of mapping the capacitance variation *via* color contrast, showing the letter shapes of "C" (e), "A" (f), and "S" (g) on the flat surface of the E-skin, and "S" (h) on the curved surface of the E-skin. The weights of the rubber pieces showing the letter shapes of "C", "A", and "S" are 1.15, 1.19, and 1.18 g.

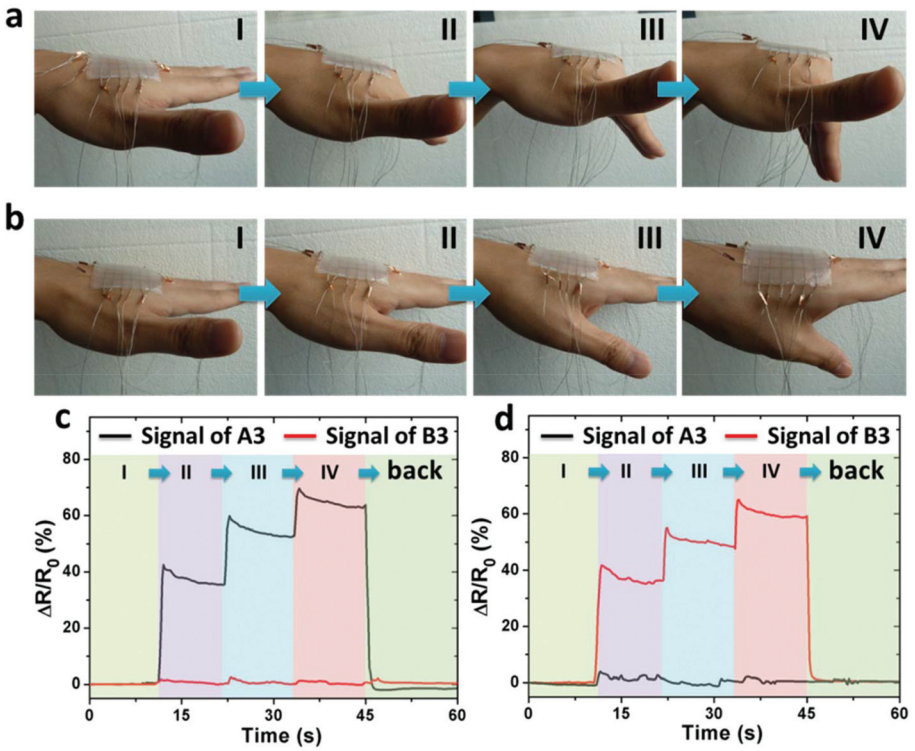

Fig. 5 The E-skin device as a wearable artificial skin for human motion monitoring. (a) Palm bending to three different stages. (b) Thumb bending to three different stages. (c) The real-time resistance variation of fiber electrodes A3 and B3 during the palm bending. (d) The real-time resistance variation of fiber electrodes A3 and B3 during the thumb bending.

seen in Fig. 4e–g. The obtained spatial distribution was in accordance with the shapes of the rubber pieces, confirming the effective pressure mapping capability of our E-skin device. Note that the response signal crosstalk (influence of the pressure on the nearby sensing pixels) could be mitigated effectively by using a D-layer with a higher elastic modulus, which restrained the pressure extension around the pressing position at the expense of signal strength (detailed information in Fig. S10, ESI†).

Furthermore, the pressure sensing function of the E-skin was also tested under a curvature state to evaluate its reliability in applications where the E-skin sensor needs to be deployed on curvilinear substrates, such as prosthetics, humanoid robots, and human wearable devices. As shown in Fig. 4d, the E-skin was adhered conformably onto the outer surface of a round glass bottle (diameter of 3 cm), and the rubber piece of "S" was placed upon the E-skin (Fig. 4d). Similarly, the spatial pressure distribution was mapped in Fig. 4h, which clearly displayed the contacting positions of the rubber piece with the E-skin.

Besides the utilization as a pressure sensing platform, the E-skin could also be exploited as a wearable artificial skin to monitor human motions *via* detecting the human skin strain induced by joint movements. As a proof-of-concept demonstration, the E-skin was adhered conformably and tightly onto the surface of the back of human hand (schematic of the numbering of the fiber electrodes in Fig. S11, ESI†). When the palm (Fig. 5a) and the thumb (Fig. 5b) bended in three different stages (from stage I to stages II, III, and IV), respectively, the real-time resistance variation of fiber electrodes A3 and B3 was recorded. As seen in Fig. 5c, as the palm bended forward, the skin strain induced by the joint movement was mainly along the direction of the index finger, which was transferred to the E-skin and caused the resistance variation of fiber electrode A3. At the same time, the resistance of fiber electrode B3 stayed almost constant as hardly any skin strain perpendicular to the index finger occurred. The skin strain direction was just opposite to the thumb bending situation, as revealed in Fig. 5d. In this way, the E-skin successfully served as a wearable artificial skin capable of monitoring and distinguishing the joint-movement-related human motions.

3. Conclusion

In summary, we skillfully made a combination of rational structure design and engineered sensing materials, to achieve an intrinsically stretchable and highly sensitive E-skin sensor. The E-skin possessed the capability of detecting multiple mechanical stimuli, including pressure, proximity, and lateral strain. The optimized D-layer allowed a wide dynamic sensing range of up to 50 kPa and a detection limit of 1.5 Pa. In proximity sensing, the E-skin could effectively "see" the approaching human finger from above within 20 cm. Also remarkably, the strain sensing properties of the pre-cracked fiber electrodes and the orthogonally aligned configuration synergistically enabled the E-skin to capture the lateral strain and determine the strain direction. The utilization of the E-skin as a pressure sensing platform and wearable artificial skin for human motion monitoring was demonstrated, thus making our E-skin sensor a highly promising candidate in future applications such as human–machine interactions, smart prosthetics, and humanoid robots.

4. Experimental section

The fabrication of the pre-cracked fiber electrodes

SCY (~350 μm in diameter) is commercially available in the textile market. The SCY was first cleaned ultrasonically in deionized water for 10 min and then dried in air. The SCY was then dipped into a condensed AgNW dispersion in ethylene glycol (average length of 20 μm, diameter of 120 nm, 20 mg mL^{-1}, from XFNANO Corporation) for 5 s and immediately dried using a blow dryer. The dip-coating could be repeated as needed to tune the conductivity. The SCY-AgNW fiber with 5 dip-coating times was selected in the following fabrication of pre-cracked fiber electrodes. After this, the SCY with AgNW coating went through an annealing treatment in an oven (100 °C, 10 min) to weld the junctions of the AgNW network. To generate evenly distributed cracks on the surface of the AgNW film, the SCY-AgNW fiber was stretched to a strain of 40% and then released.

The assembly of the E-skin device

The wearable and stretchable E-skin was fabricated through a layer-by-layer assembly strategy. First, liquid PDMS (ratio of base to crosslinker, 10 : 1 by mass, Dow Corming Sylgard 184) was mixed, degassed, and poured onto a Si-wafer and then cured in an oven (80 °C, 2 hours), to obtain a S-layer with a thickness of 270 μm. Then pre-cracked fiber electrodes were aligned in parallel (6 fibers with a pitch size of 5 mm) on the S-layer, and a liquid polymer of PDMS, Dragon skin 10 (Smooth-on Corporation), or Ecoflex 00-30 (Smooth-on Corporation) was poured on the S-layer to just submerge the pre-cracked fiber electrodes and cured (for PDMS, 80 °C, 2 hours; for Dragon skin, 60 °C, 10 min; for Ecoflex 00-30, 60 °C, 10 min) as an E-layer with a thickness of 350 μm. Finally, the liquid polymer of PDMS, Dragon skin 10, or Ecoflex 00-30 was spin-coated on the E-layer as a D-layer with a thickness of 75 μm. Before complete curing of this D-layer, another E-layer was attached face to face above orthogonally. To ensure the homogeneity of the layer thickness, a blading assisted method was adopted to further smoothen the surface after the liquid polymer was coated (detailed information in Fig. S12, ESI†). After curing (for PDMS, 80 °C, 2 hours; for Dragon skin, 60 °C, 10 min; for Ecoflex 00-30, 60 °C, 10 min), the multilayered E-skin device was obtained. Herein, the materials used for the D-layer and E-layer were the same to enhance the bonding force at the interface. For capacitance and resistance measuring, the two ends of each of the pre-

cracked fiber electrodes were connected with copper wires with the aid of Ag paste and copper tapes.

The durability test of pressure sensing capability of the E-skin

The test the durability of pressure sensing, the E-skin was attached and fixed onto a rigid and vertical glass plate against a wall. A high-precision motorized linear stage (displacement resolution of 2.5 μm) was placed and fixed in front of the E-skin. A customized force gauge (Mark-10 M4-012 Force Gauge) containing a long plastic pole terminated with a square-shaped glass sheet (5 mm × 5 mm) was fixed onto the motorized linear stage. The motorized linear stage was programmed to press the center of a sensing pixel in the E-skin using the force gauge for up to 10 000 cycles, with the maximal pressure of 13.7 kPa. The capacitance of the sensing pixel was measured at pressures of 0.84 and 13.7 kPa after specific loading cycles.

The determination of the strain sensing response time

To obtain the response time of strain sensing, a quasi-transient step strain of 1% was input to the Eskin along the axial direction of the fiber electrode using a high-precision electronic universal testing machine (CMT6103, MTS Systems (China) Co., Ltd). During the process, a constant voltage (0.01 V) was loaded on the fiber electrode to acquire a real-time (time resolution of 5 ms) current signal, using an electrochemical workstation (PARSTAT 2273, Princeton Applied Research), to record the real-time resistance variation.

The fabrication process of the disk-shaped E-layer

To test the multidirectional stain sensing properties of the E-skin, a disk-shaped E-layer was designed. The fabrication process was similar to that of the E-skin. First, a fiber electrode was fixed onto the surface of the S-layer (cut to a disk shape). Then the polymer liquid of Ecoflex 00-30 was poured onto the S-layer to just submerge the fiber electrode and then cured (80 °C, 10 min). After that, a small amount of liquid Ecoflex 00-30 was spin-coated onto the surface of the E-layer and another disk shaped S-layer was attached above, followed by curing (80 °C, 10 min) to obtain a disk-shaped E-layer. The two ends of the fiber electrode were left out to allow the connection with the copper wire for measuring the resistance.

Characterization

The SEM characterization was accomplished using a Hitachi SU8200 FE-SEM. In the pressure sensing test, the pressure was applied using a customized force gauge (low pressure range: Mark-10, M4-012; high pressure range: Handpi Digital force gauge, HP5) fixed onto a high-precision electronic universal testing machine (CMT6103, MTS Systems (China) Co., Ltd), except that the durability test was implemented with the aid of a high-precision motorized linear stage (displacement resolution of 2.5 μm). The capacitance of the E-skin was measured by using a LCR tester (IM3536, HIOKI, Japan). In the strain sensing performance testing, the strain was applied using a high-precision electronic universal testing machine (CMT6103, MTS Systems (China) Co., Ltd), except that the durability test was conducted using a high-precision motorized linear stage (displacement resolution of 2.5 μm).

Acknowledgements

This work was financially supported by the Shanghai Science and Technology Star Project, Youth Innovation Promotion Association CAS (2014226), the Shanghai Key Basic Research Project (16JC1402300), the Major State Research Development Program of China (2016YFA0203000) and the State Key Lab of High Performance Ceramics and Superfine Microstructure Director fund.

References

1 B. C. Tee, C. Wang, R. Allen and Z. Bao, *Nat. Nanotechnol.*, 2012, **7**, 825–832.
2 C. Pang, G.-Y. Lee, T.-i. Kim, S. M. Kim, H. N. Kim, S.-H. Ahn and K.-Y. Suh, *Nat. Mater.*, 2012, **11**, 795–801.
3 L. Y. Chen, B. C. Tee, A. L. Chortos, G. Schwartz, V. Tse, D. J. Lipomi, H. S. Wong, M. V. McConnell and Z. Bao, *Nat. Commun.*, 2014, **5**, 5028.
4 Y.-C. Lai, B.-W. Ye, C.-F. Lu, C.-T. Chen, M.-H. Jao, W.-F. Su, W.-Y. Hung, T.-Y. Lin and Y.-F. Chen, *Adv. Funct. Mater.*, 2016, **26**, 1286–1295.
5 S. Lim, D. Son, J. Kim, Y. B. Lee, J.-K. Song, S. Choi, D. J. Lee, J. H. Kim, M. Lee, T. Hyeon and D.-H. Kim, *Adv. Funct. Mater.*, 2015, **25**, 375–383.
6 A. P. Gerratt, H. O. Michaud and S. P. Lacour, *Adv. Funct. Mater.*, 2015, **25**, 2287–2295.
7 J. W. Zhong, H. L. Zhu, Q. Z. Zhong, J. Q. Dai, W. B. Li, S. H. Jang, Y. G. Yao, D. Henderson, Q. Y. Hu, L. B. Hu and J. Zhou, *ACS Nano*, 2015, **9**, 7399–7406.
8 M. Y. Shi, J. X. Zhang, H. T. Chen, M. D. Han, S. A. Shankaregowda, Z. M. Su, B. Meng, X. L. Cheng and H. X. Zhang, *ACS Nano*, 2016, **10**, 4083–4091.
9 S. Choi, H. Lee, R. Ghaffari, T. Hyeon and D. H. Kim, *Adv. Mater.*, 2016, **28**, 4203–4218.
10 M. L. Hammock, A. Chortos, B. C. Tee, J. B. Tok and Z. Bao, *Adv. Mater.*, 2013, **25**, 5997–6038.
11 G. Westling and R. S. Johansson, *Exp. Brain Res.*, 1984, **53**, 277–284.
12 R. S. Johansson and J. R. Flanagan, *Nat. Rev. Neurosci.*, 2009, **10**, 345–359.
13 G. Y. Bae, S. W. Pak, D. Kim, G. Lee, H. Kim do, Y. Chung and K. Cho, *Adv. Mater.*, 2016, **28**, 5300–5306.
14 C. L. Choong, M. B. Shim, B. S. Lee, S. Jeon, D. S. Ko, T. H. Kang, J. Bae, S. H. Lee, K. E. Byun, J. Im, Y. J. Jeong, C. E. Park, J. J. Park and U. I. Chung, *Adv. Mater.*, 2014, **26**, 3451–3458.
15 Z. Lou, S. Chen, L. Wang, K. Jiang and G. Shen, *Nano Energy*, 2016, **23**, 7–14.

16 S. Gong, W. Schwalb, Y. Wang, Y. Chen, Y. Tang, J. Si, B. Shirinzadeh and W. Cheng, *Nat. Commun.*, 2014, **5**, 3132.
17 J. Chun, K. Y. Lee, C.-Y. Kang, M. W. Kim, S.-W. Kim and J. M. Baik, *Adv. Funct. Mater.*, 2014, **24**, 2038–2043.
18 L. Dhakar, P. Pitchappa, F. E. H. Tay and C. Lee, *Nano Energy*, 2016, **19**, 532–540.
19 F. R. Fan, L. Lin, G. Zhu, W. Wu, R. Zhang and Z. L. Wang, *Nano Lett.*, 2012, **12**, 3109–3114.
20 B. Zhang, Z. Xiang, S. Zhu, Q. Hu, Y. Cao, J. Zhong, Q. Zhong, B. Wang, Y. Fang, B. Hu, J. Zhou and Z. Wang, *Nano Res.*, 2014, **7**, 1488–1496.
21 Y. Joo, J. Byun, N. Seong, J. Ha, H. Kim, S. Kim, T. Kim, H. Im, D. Kim and Y. Hong, *Nanoscale*, 2015, **7**, 6208–6215.
22 J. Wang, J. Jiu, M. Nogi, T. Sugahara, S. Nagao, H. Koga, P. He and K. Suganuma, *Nanoscale*, 2015, **7**, 2926–2932.
23 S. Yao and Y. Zhu, *Nanoscale*, 2014, **6**, 2345–2352.
24 D. J. Lipomi, M. Vosgueritchian, B. C. K. Tee, S. L. Hellstrom, J. A. Lee, C. H. Fox and Z. Bao, *Nat. Nanotechnol.*, 2011, **6**, 788–792.
25 J. Lee, H. Kwon, J. Seo, S. Shin, J. H. Koo, C. Pang, S. Son, J. H. Kim, Y. H. Jang, D. E. Kim and T. Lee, *Adv. Mater.*, 2015, **27**, 2433–2439.
26 S. C. Mannsfeld, B. C. Tee, R. M. Stoltenberg, C. V. Chen, S. Barman, B. V. Muir, A. N. Sokolov, C. Reese and Z. Bao, *Nat. Mater.*, 2010, **9**, 859–864.
27 T. Yamada, Y. Hayamizu, Y. Yamamoto, Y. Yomogida, A. Izadi-Najafabadi, D. N. Futaba and K. Hata, *Nat. Nanotechnol.*, 2011, **6**, 296–301.
28 J. J. Park, W. J. Hyun, S. C. Mun, Y. T. Park and O. O. Park, *ACS Appl. Mater. Interfaces*, 2015, **7**, 6317–6324.
29 Y. Cheng, R. Wang, J. Sun and L. Gao, *Adv. Mater.*, 2015, **27**, 7365–7371.
30 L. Cai, L. Song, P. Luan, Q. Zhang, N. Zhang, Q. Gao, D. Zhao, X. Zhang, M. Tu, F. Yang, W. Zhou, Q. Fan, J. Luo, W. Zhou, P. M. Ajayan and S. Xie, *Sci. Rep.*, 2013, **3**, 3048.
31 Q. Liu, J. Chen, Y. Li and G. Shi, *ACS Nano*, 2016, **10**, 7901–7906.
32 S. Ryu, P. Lee, J. B. Chou, R. Z. Xu, R. Zhao, A. J. Hart and S. G. Kim, *ACS Nano*, 2015, **9**, 5929–5936.
33 U.-H. Shin, D.-W. Jeong, S.-M. Park, S.-H. Kim, H. W. Lee and J.-M. Kim, *Carbon*, 2014, **80**, 396–404.
34 M. Kollosche, H. Stoyanov, S. Laflamme and G. Kofod, *J. Mater. Chem.*, 2011, **21**, 8292.
35 X. Wang, T. Li, J. Adams and J. Yang, *J. Mater. Chem. A*, 2013, **1**, 3580.
36 D. J. Cohen, D. Mitra, K. Peterson and M. M. Maharbiz, *Nano Lett.*, 2012, **12**, 1821–1825.
37 T. Li, H. Luo, L. Qin, X. Wang, Z. Xiong, H. Ding, Y. Gu, Z. Liu and T. Zhang, *Small*, 2016, **12**, 5042–5048.
38 J. Kim, M. Lee, H. J. Shim, R. Ghaffari, H. R. Cho, D. Son, Y. H. Jung, M. Soh, C. Choi, S. Jung, K. Chu, D. Jeon, S. T. Lee, J. H. Kim, S. H. Choi, T. Hyeon and D. H. Kim, *Nat. Commun.*, 2014, **5**, 5747.
39 S. Harada, K. Kanao, Y. Yamamoto, T. Arie, S. Akita and K. Takei, *ACS Nano*, 2014, **8**, 12851–12857.
40 L. Hu, M. Pasta, F. L. Mantia, L. Cui, S. Jeong, H. D. Deshazer, J. W. Choi, S. M. Han and Y. Cui, *Nano Lett.*, 2010, **10**, 708–714.
41 X. Liu, H. Chang, Y. Li, W. T. Huck and Z. Zheng, *ACS Appl. Mater. Interfaces*, 2010, **2**, 529–535.
42 Y. J. Yun, W. G. Hong, W. J. Kim, Y. Jun and B. H. Kim, *Adv. Mater.*, 2013, **25**, 5701–5705.
43 Y. Cheng, R. Wang, J. Sun and L. Gao, *ACS Nano*, 2015, **9**, 3887–3895.
44 I. D. Johnston, D. K. McCluskey, C. K. L. Tan and M. C. Tracey, *J. Micromech. Microeng.*, 2014, **24**, 035017.
45 B. C. K. Tee, A. Chortos, R. R. Dunn, G. Schwartz, E. Eason and Z. Bao, *Adv. Funct. Mater.*, 2014, **24**, 5427–5434.
46 M. Ha, S. Lim, J. Park, D.-S. Um, Y. Lee and H. Ko, *Adv. Funct. Mater.*, 2015, **25**, 2841–2849.
47 W. Zhong, Q. Liu, Y. Wu, Y. Wang, X. Qing, M. Li, K. Liu, W. Wang and D. Wang, *Nanoscale*, 2016, **8**, 12105–12112.
48 S. Y. Kim, S. Park, H. W. Park, D. H. Park, Y. Jeong and D. H. Kim, *Adv. Mater.*, 2015, **27**, 4178–4185.
49 W. Wu, X. Wen and Z. L. Wang, *Science*, 2013, **340**, 952–957.
50 D. Kang, P. V. Pikhitsa, Y. W. Choi, C. Lee, S. S. Shin, L. Piao, B. Park, K.-Y. Suh, T.-i. Kim and M. Choi, *Nature*, 2014, **516**, 222–226.
51 W. Wang, T. Yang, H. Zhu and Q. Zheng, *Appl. Phys. Lett.*, 2015, **106**, 171903.
52 B. Park, J. Kim, D. Kang, C. Jeong, K. S. Kim, J. U. Kim, P. J. Yoo and T. I. Kim, *Adv. Mater.*, 2016, **28**, 8130–8137.
53 M. Amjadi, A. Pichitpajongkit, S. Lee, S. Ryu and I. Park, *ACS Nano*, 2014, **8**, 5154–5163.
54 K. K. Kim, S. Hong, H. M. Cho, J. Lee, Y. D. Suh, J. Ham and S. H. Ko, *Nano Lett.*, 2015, **15**, 5240–5247.

